Phenomenological Model of Thermal Shock Propagation in Ceramic Monolith

L. Boshoff-Mostert, S. Schroeder, N. F. J. van Rensburg, and H. J. Viljoen
Dept. of Chemical Engineering, University of Nebraska-Lincoln, Lincoln, NE 68588

A discrete model is used to study the behavior of shock propagation, crack formation, and crack propagation of a thin ceramic plate. This plate represents a wall of a channel in a monolithic structure. The model involves a spring-node formulation on a rectangular geometry, which approaches the continuum model correctly when the Poisson ratio is taken as 0.25. Viscous damping is also included. Shock waves originate from perturbations due to local ignition (hot spots), sudden quenching or other changes in operating and driving conditions. The shock wave propagates from the perturbed region. Internodal displacements are used to calculate strains, and the values are compared to a maximum strain associated with failure. Spring constants are set to zero when the maximum strain is exceeded. Reflection of compressional waves from free boundaries as tensional waves leads to enhanced crack formation near the free boundary. Shock waves attenuate much faster when the plate is precracked. Propagation velocities are lower for precracked plates, due to a decrease in (effective) Young's modulus. Velocities of pure compressional and shear waves compare quite well with theoretical values.

Introduction

Ceramic materials are visible contenders for material selection in engineering systems with high-temperature demands. The use of ceramic materials is evident especially for the automotive industry in the design and manufacture of monolithic reactors, widely used as catalytic converters in automobile emission control (Taylor, 1984; Zygourakis, 1989; Leclerc and Schweich, 1993). The monolith consists of a honeycomb structure (support) whose parallel channels are coated with a thin layer of porous catalyst carrier impregnated with the active catalytic material (Villermaux and Schweich, 1994). Ceramics often used as support media are commercially available as cordierite or α-alumina (corundum). When light-off occurs or during transient operation of the monolith, strong thermal gradients develop in the structure and these gradients play a causal role in thermal stresses. A fundamental characteristic of ceramic materials is that they show no plastic deformations before failure, and they have little toughness to arrest cracks. Most ceramic materials, because of inherent brittleness, are susceptible to catastrophic fracture under thermal shocks (Kam and Lu, 1989). It has long been presumed that certain flaws, particularly processing defects, are inevitably susceptible to spontaneous failure when the single value critical stress of the material is exceeded (Bennison and Lawn, 1989). Hasselman (1969) analyzed the effect of microcracks on strength and Young's modulus. He showed that existing cracks can actually facilitate an appreciable increase in the strain at fracture, hence increasing thermal shock resistance. The mechanism for microcrack toughening is twofold. Microcracks first relieve residual tensile stresses of a propagating flaw acting as stress concentrators. Secondly, the surrounding matrix of a microcrack is more elastic than the surrounding uncracked matrix. This effective modulus modification may shield the flaw from the applied stress field (Curtin and Futamura, 1990). They calculated R-curves, crack-tip stresses, and average crack tip shielding and found the results to be in good agreement with results of continuum models.

The model presented here offers a phenomenological study of thermal shock propagation in elastic ceramic supports. The main focus of the study is to investigate the influence of a thermal shock on a ceramic monolith. The smallest repetitive element of such a structure is a single wall, which will form the basis of our study. An existing crack distribution in the monolith has a marked influence on the propagation and at-

Correspondence concerning this article should be addressed to H. J. Viljoen.
Current address of N. F. J. van Rensburg: Dept. of Mathematics, University of Pretoria, South Africa.

tenuation of shock waves and on the crack propagation. In the present stress and strain formulation, we approximate the continuous medium (i.e., a channel wall) by a system of nodes and springs. A thermal shock resulting in crack formation is administered to both a flawless (in the sense of no initial cracks) and precracked (i.e., having an existing crack distribution) specimen and qualitative results are obtained.

There are several advantages to model crack propagation by a spring node model (SNM), and the formation of cracks and their forms (obviously limited by the coarseness of discretization) are handled very easily—this is not a simple task in the continuum model. Secondly, the redistribution of the load in a cracked system is taken care of by the formulation; in the continuum model the stress concentration at crack tips (of order $(1/\sqrt{\text{crack tip radius}})$ requires special attention (Cherepanov, 1979). There are several other applications of the SNM which are of importance to chemical engineers. A fundamental description of metal oxidation involves transport of species across a film. Stresses develop in these films which can lead to fracture and changes in the oxidation rate. Although fracture of protective films often occurs during corrosion, the model is especially suitable for modeling combustion of metallic powders. Researchers are also very interested in the improvement of fracture toughness of materials and the adjustment of R-curve characteristics. The SNM can be used to study shock wave or crack propagation in the presence of fibers, platelets, inclusions of a second phase, or materials with graded properties. However, it must be kept in mind that this is a phenomenological model that compliments and does not compete with quantitative models.

Model Formulation

The smallest repetitive unit in a monolith channel is a single wall. The wall has a thickness Δt (m) which is much smaller than the height and length of the wall, and changes in the thickness during loading will be neglected. The wall is modeled by $N \times M$ equidistant nodes connected with springs, as shown in Figure 1. Internodal distances are Δx and Δy, and these values are equal when an equidistant mesh is used. Spring constants in the x and y directions are denoted k (N/m) and in the diagonal direction as q (N/m). Each node is initially at rest in its equilibrium position $(xe_{i,j}; ye_{i,j})$, and no net forces exist in the system.

Consider a point (i, j) in the wall. The mass is concentrated in the nodes, and the mass at (i, j) is

$$m_{i,j} = \rho \Delta x \Delta y \Delta t \tag{1}$$

Nodes will move from their equilibrium position if they experience a net force, and after the perturbation the node will be at the position $(x_{i,j}; y_{i,j})$. This leads to the definition of the displacement vector

$$(u_{i,j}; v_{i,j}) = (x_{i,j} - xe_{i,j}; y_{i,j} - ye_{i,j}) \tag{2}$$

We use a linear elastic model to describe the monolith behavior. Therefore, the displacements must be small in the absolute sense and in the linear region of deformation Hooke's law is applicable. In a local numbering system, the diagonal

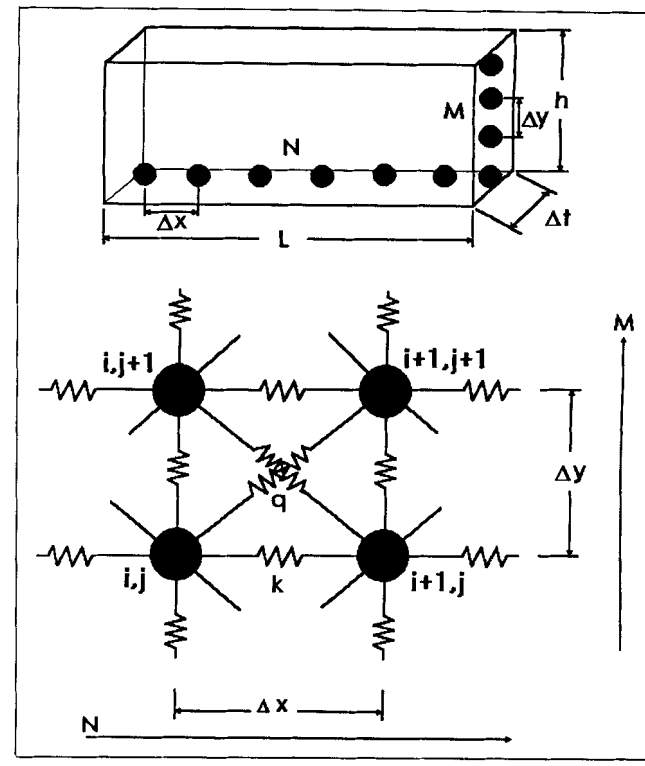

Figure 1. Spring node model.

springs around node (i, j) are labeled clockwise starting at the diagonal spring between (i, j) and $(i+1, j+1)$, i.e., $q_1 \ldots q_4$. We also label the longitudinal and transversal springs clockwise starting at the spring between (i, j) and $(i+1, j)$. A displacement from the equilibrium positions will introduce a change in the diagonal, longitudinal, and transversal distances. Although it is simple to evaluate these changes, it is perhaps instructive to show the diagonal case. Considering q_1 and neglecting the second-order terms, the net diagonal displacement (m) is

$$ds_1 = \frac{\Delta x}{\sqrt{\Delta x^2 + \Delta y^2}}[u_{i+1,j+1} - 2u_{i,j}] + \frac{\Delta y}{\sqrt{\Delta x^2 + \Delta y^2}}[v_{i+1,j+1} - 2v_{i,j}]. \tag{3}$$

Since we use an equidistant mesh, $\Delta x = \Delta y$. The x and y-components of ds_1 are

$$ds_{x1} = ds_{y1} = \frac{1}{2}[u_{i+1,j+1} - u_{i,j} + v_{i+1,j+1} - v_{i,j}]. \tag{4}$$

Likewise, the components can be determined for the other three springs

$$ds_{x2} = \frac{1}{2}[u_{i+1,j-1} - u_{i,j} - v_{i+1,j-1} + v_{i,j}]. \tag{5}$$

$$ds_{x3} = \frac{1}{2}[u_{i-1,j-1} - u_{i,j} + v_{i-1,j-1} - v_{i,j}]. \tag{6}$$

$$ds_{x4} = \frac{1}{2}[u_{i-1,j+1} - u_{i,j} - v_{i-1,j+1} + v_{i,j}]. \quad (7)$$

In terms of the displacement vector, the balance of forces in the x-direction gives

$$\rho \Delta x \Delta y \Delta t \frac{\partial^2 u_{i,j}}{\partial t^2} = k_1[u_{i+1,j} - u_{i,j}] + k_3[u_{i-1,j} - u_{i,j}] + \sum_{l=1,4} q_l ds_{xl} \quad (8)$$

and in the y-direction

$$\rho \Delta x \Delta y \Delta t \frac{\partial^2 v_{i,j}}{\partial t^2} = k_2[v_{i,j-1} - v_{i,j}] + k_4[v_{i,j+1} - v_{i,j}] + \sum_{l=1,4} q_l ds_{yl} \quad (9)$$

In an isotropic system the spring constants k_l are all the same and q_l are all the same.

To model acoustic fields with lossless propagation is an idealism. Attentuation can be included in the formulation by assuming that viscous damping is the dominant process (Auld, 1982, p. 86). The damping forces (N) in the x and y-directions are given by

$$F_{dx} = C\frac{\partial}{\partial t}[u_{i+1,j} - 2u_{i,j} + u_{i-1,j}] \quad (10)$$

$$F_{dy} = C\frac{\partial}{\partial t}[v_{i,j+1} - 2v_{i,j} + v_{i,j-1}] \quad (11)$$

and they are included in the formulation. Strictly speaking C is a fourth rank tensor, but we do not consider the damping of shear modes.

The equations are written in dimensionless form by defining the following variables

$$\chi_{i,j} = \frac{u_{i,j}(N-1)}{L}, \quad \gamma_{i,j} = \frac{v_{i,j}(M-1)}{h}, \quad \tau = t/T_r,$$

$$\kappa = \frac{k}{k_s}, \quad Q = \frac{q}{k_s} \quad \text{and} \quad \xi = \frac{C}{\sqrt{(k_s m)/\Delta t^2}}.$$

The values of the parameters are listed in Table 1. It is not evident from Eqs. 10–11 how breakage of springs affects the damping terms. First, define

$$p_{i,j,l} = \begin{cases} 1, & k_l > 0 \\ 0, & k_l = 0. \end{cases}$$

The equations can be written for each internal node as follows

Table 1. Parameter Values

Item	Units	Value
C	Ns/m^2	0.1
E_Y	GPa	400
k_s	—	$(0.8E_Y\Delta t)/400$
M	—	21
N	—	250
Δt	m	125×10^{-6}
ν	—	0.25
ρ	kg/m^3	4,000

$$\frac{d^2\chi_{i,j}}{d\tau^2} = \kappa_1[\chi_{i+1,j} - \chi_{i,j}] + \kappa_3[\chi_{i-1,j} - \chi_{i,j}] + \frac{Q_1}{2}[\chi_{i+1,j+1} - \chi_{i,j} + \gamma_{i+1,j+1} - \gamma_{i,j}] + \frac{Q_2}{2}[\chi_{i+1,j-1} - \chi_{i,j} - \gamma_{i+1,j-1} + \gamma_{i,j}] + \frac{Q_3}{2}[\chi_{i-1,j-1} - \chi_{i,j} + \gamma_{i-1,j-1} - \gamma_{i,j}] + \frac{Q_4}{2}[\chi_{i-1,j+1} - \chi_{i,j} - \gamma_{i-1,j+1} + \gamma_{i,j}] - \xi\frac{d}{d\tau}[p_{i,j,1}(\chi_{i+1,j} - \chi_{i,j}) + p_{i,j,3}(\chi_{i-1,j} - \chi_{i,j})] \quad (12)$$

$$\frac{d^2\gamma_{i,j}}{d\tau^2} = \kappa_2[\gamma_{i,j-1} - \gamma_{i,j}] + \kappa_4[\gamma_{i,j+1} - \gamma_{i,j}] + \frac{Q_1}{2}[\chi_{i+1,j+1} - \chi_{i,j} + \gamma_{i+1,j+1} - \gamma_{i,j}] + \frac{Q_2}{2}[\chi_{i+1,j-1} - \chi_{i,j} - \gamma_{i+1,j-1} + \gamma_{i,j}] + \frac{Q_3}{2}[\chi_{i-1,j-1} - \chi_{i,j} + \gamma_{i-1,j-1} - \gamma_{i,j}] + \frac{Q_4}{2}[\chi_{i-1,j+1} - \chi_{i,j} - \gamma_{i-1,j+1} + \gamma_{i,j}] - \xi\frac{d}{d\tau}[p_{i,j,4}(\gamma_{i,j+1} - \gamma_{i,j}) + p_{i,j,3}(\gamma_{i,j+1} - \gamma_{i,j})] \quad (13)$$

We consider fixed conditions normal to the top and bottom edges of the wall. Therefore, the y-components of the displacement vectors are set to zero at the top and bottom rows of the mesh. Displacements in the x-direction are permitted. The boundary conditions at the left and right sides are traction-free. This condition implies that spring constants which correspond to the fictitious nodes outside the domain proper are set to zero.

A fourth-order Runge-Kutta method is used to solve the initial value problem. The system can be loaded in different ways. An external force can be applied, either as a body force or traction at the wall. This force will cause a perturbation in the position of a node (or nodes). The origin of this force can be mechanical or thermal. The spring constants are stored in vectors, and this enables us to follow the history of each node. Remark: An obvious application is the simulation of creep and plastic flows.

Verification of Model

It is instructive to compare our model with the continuum model and determine the relationship between the spring constants and the continuum properties E_Y (Young's modulus and ν (Poisson's ratio). If the spring-node model reduces to the continuum model in the limit $\Delta x\,\Delta y \to \infty$, it also serves as a confirmation on the validity of the approximation. Dropping the subscripts in the spring constants of Eqs. 12–13 and using Taylor expansions to express all displacements in terms of derivatives and the displacements at (i,j), one gets the acoustic equations

$$\Delta t\rho\frac{\partial^2 u_{i,j}}{\partial t^2} = k\frac{\partial^2 u_{i,j}}{\partial x^2} + q\left[2\nabla^2 u_{i,j} + 4\frac{\partial^2 v_{i,j}}{\partial x\partial y}\right] \quad (14)$$

$$\Delta t\rho\frac{\partial^2 v_{i,j}}{\partial t^2} = k\frac{\partial^2 v_{i,j}}{\partial y^2} + q\left[2\nabla^2 v_{i,j} + 4\frac{\partial^2 u_{i,j}}{\partial x\partial y}\right]. \quad (15)$$

The continuum model is (Boley and Weiner, 1960)

$$(\lambda+\mu)\frac{\partial e}{\partial x} + \mu\nabla^2\mu = \rho\frac{\partial^2 u}{\partial t^2}$$

$$(\lambda+\mu)\frac{\partial e}{\partial y} + \mu\nabla^2\nu = \rho\frac{\partial^2 \nu}{\partial t^2} \quad (16)$$

where e is the dilatation

$$e = \frac{\partial u}{\partial x} + \frac{\partial v}{\partial y}.$$

The spring-node model only matches the continuum model if the two Lame constants λ and μ are the same. This implies that the Poisson ratio should be 0.25. According to Dörre and Hübner (1984), the ν values for α-alumina lie between $\nu = 0.22$ and $\nu = 0.25$. Since the proper value for the model coincides with the suggested values, the spring constants were evaluated as

$$k = 0.8\Delta t E_Y \quad (17)$$

$$q = 0.2\Delta t E_Y. \quad (18)$$

When a perturbation is introduced at a local region of the mesh, a shock wave will propagate from this region. In solids, the particles can oscillate along the direction of wave propagation as longitudinal waves, or the oscillations can be perpendicular to the direction of traveling waves, as transverse shear waves. Since we limit the perturbations to be in the plane of the wall, only longitudinal or shear waves exist. The propagation velocities of pure compressional (e.g., x-propagating x-polarized) waves are higher than pure shear wave (e.g., x-propagating y-polarized) velocities (Cartz, 1995). As a further test of our model, we will compare the velocities of our model with the solution of the acoustic equations.

The velocities of acoustic perturbations in an elastic medium can be determined from the displacement formulation (Boley and Weiner, 1960, p. 288). For the monolith wall which is modeled as a two-dimensional slab, these equations take the form

$$(\lambda+\mu)\frac{\partial e}{\partial x} + \mu\nabla^2 u - (3\lambda+2\mu)\alpha\frac{\partial T_w}{\partial x} = \rho\frac{\partial^2 u}{\partial t^2} - C\frac{\partial^3 u}{\partial t\partial x^2} \quad (19)$$

$$(\lambda+\mu)\frac{\partial e}{\partial y} + \mu\nabla^2 v - (3\lambda+2\mu)\alpha\frac{\partial T_w}{\partial y} = \rho\frac{\partial^2 v}{\partial t^2} - C\frac{\partial^3 v}{\partial t\partial y^2}. \quad (20)$$

The temperature plays the role of a nonhomogeneous term in these equations (on the time scale of acoustic perturbations, the temperature field is stationary). The acoustic equations are linear and the solution can be split into a dynamic and a stationary part. The stationary displacement solution satisfies the static thermal stress problem, while the dynamic part is damped out. When stationary forces are applied to the system, the dynamic solution will approach a steady state consistent with these forces. In this study we concentrate on the dynamic behavior of the system after it has been perturbed by a local impulse.

In order to compare the velocities of the continuous model and the spring-node model, first consider a compressional wave of the form

$$u = Ae^{\omega\tau + ik_x x} \quad (21)$$

$$v = 0. \quad (22)$$

Upon substitution of this form into Eqs. 19–20, the following dispersion relation is found

$$(\lambda+2\mu)k_x^2 + \rho\omega^2 + \omega k_x^2 C = 0. \quad (23)$$

Since the variable ω is complex, Eq. 23 can be split into real and imaginary parts and solved separately. The displacements are damped with time by the real part of ω.

$$\omega_R = -\frac{k_x^2 C}{2\rho} \quad (24)$$

The velocity of the compressional wave (m/s) is given by

$$v_c = \frac{\omega_I}{k_x} = \sqrt{\frac{(\lambda+2\mu) - \dfrac{k_x^2 C^2}{4\rho}}{\rho}}. \quad (25)$$

The mesh consists of 21 rows and 250 columns. In order to perturb the system to create a purely compressional wave, the initial position of all nodes between columns 100 and 120 are displaced only along the x-direction. If the perturbation is not imposed over all the rows, secondary shear waves will be created (Poisson effect). The perturbation for the compressional wave is

$$\chi_{i,j} = 0.00015\sin(2\pi(j-100)/20) \quad j = 1, 21$$
$$i = 100, \ldots, 120. \quad (26)$$

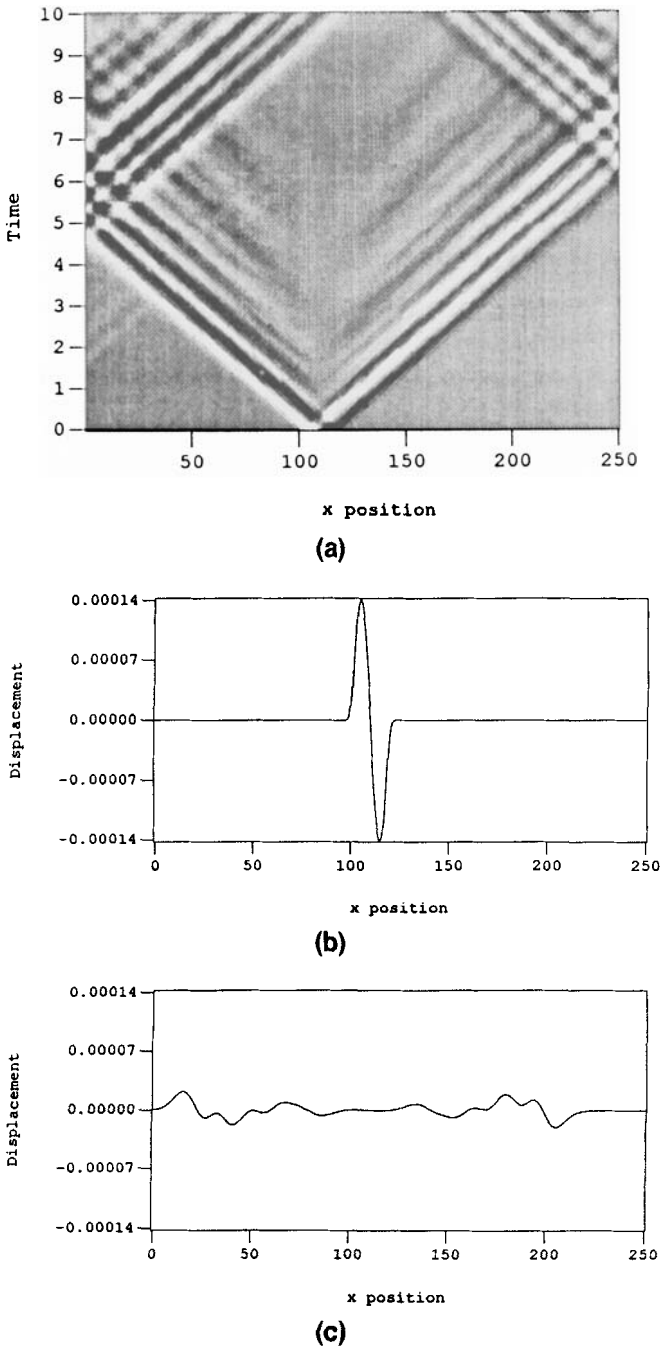

Figure 2. (a) Compressional wave; (b) initial perturbation for compressional wave ($\tau = 0^+$); (c) shock wave at $\tau = 4.5$.

The numerical results show that the wave is indeed purely compressional, because the vertical displacements were negligible. For example, $\gamma_{i,11}$, the nondimensional y displacements along the center row, were of $O(10^{-13})$.

In Figure 2a, the x-component of the displacement vector at the center row of the plate ($\chi_{i,11}$) is shown for the compressional wave in the $x \times \tau$ plane. The perturbation did not exceed the criterion for cracking (cf., Results Section). At time $\tau = 0^+$, the perturbation can be seen in Figure 2b. Left and right traveling waves propagate from the perturbed region and towards the sides. The left side is reached just after $\tau = 4.5$, as seen in Figure 2c. The incident waves are reflected and interference patterns develop. The waves are evanescent, which is apparent from the diminishing amplitudes. As time progresses, the waves propagate throughout the domain. Damping also causes a decrease in the amplitudes. The velocity can be calculated from the slope of a characteristic. The compressional velocities of the model and the dispersion relation are respectively

$$v_{c\,\text{model}} = 10{,}400 \text{ m/s}$$

$$v_c = 10{,}945 \text{ m/s}.$$

A pure shear wave (x-propagating y-polarized) is presented by the displacements

$$v = Ae^{\omega\tau + ik_x x} \tag{27}$$

$$u = 0. \tag{28}$$

Substituting these forms into Eqs. 19–20 leads to the dispersion relation

$$\frac{\omega_I}{k_x} = \sqrt{\frac{\mu}{\rho}}. \tag{29}$$

Note that the damping coefficient is not present in this expression, since the damping of shear modes has been neglected. A shear wave is induced by a perturbation of the form

$$\gamma_{j,11} = 0.00015 \sin[2\pi(j-100)/20] \quad j = 1,21 \quad i = 100 \ldots 120.$$

The boundary conditions at the top and bottom have been changed from fixed to free. In Figure 3 $\gamma_{j,11}$ is shown in the $x \times \tau$ plane. Reflection and interference can be observed for these waves, too. The difference between the shear and compression wave patterns is quite clear. The velocities given by the model and the dispersion relation (Eq. 29) can be compared

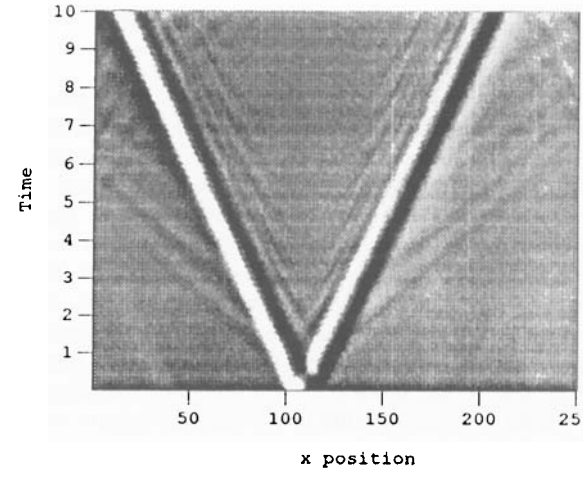

Figure 3. Shear wave.

$$v_{s\,\text{model}} = 5{,}600 \text{ m/s}$$

$$v_s = 6{,}324 \text{ m/s}.$$

The values for the SNM are subject to some errors. It is not easy to assess the exact position of the wave front after some time has elapsed. The maximum perturbation is usually preceded by a smaller one in the opposite direction. This problem is also encountered in experimental studies, and experimentalists use the cross-correlation method to determine the position of one wave relative to another. Considering these limitations, the agreement between SNM values and the continuum model is good.

Results

The SNM model lends itself to several interesting studies. It can be used to model inplane vibrations of shells, plates, or thin-wall structures. When the model is used to study the formation of cracks and crack propagation, the limitations of this model should be kept in mind (Curtin and Scher, 1990a,b). If microcracks are associated with the snapping of single springs, all microcracks will be of the same length. Furthermore, these cracks can have only certain orientations. However, as we have shown in the previous section and from results of other researchers who had used this model, the SNM can be used as a phenomenological model to study these processes.

Crack formation is modeled by setting the spring constant to zero whenever the strain between two nodes exceeds the maximum strain value. This value is obtained by dividing the fracture strength by E_Y. Prantskyavichyus (1987) reported an experimental bending strength of 254 MPa which can be related to tensile strength by dividing by $\sqrt{3}$ to give a value of 146.6 MPa. Coble and Kingery (1956) studied the tensile strength of alumina at 750°C for different porosities. For 17% porosity, which is typical for catalyst supports, the tensile strength is 104 MPa. Coble and Parikh (1972) also presented an expression to relate the tensile strength with grain size and porosity. From these studies, a value of 100 MPa was chosen for the tensile strength. The maximum strain is

$$\epsilon_{\max} = \frac{100 \text{ MPa}}{4 \times 10^5 \text{ MPa}} = 250 \times 10^{-6}\ \epsilon. \tag{30}$$

Note that strain between nodes (i, j) and $(i+1, j)$, for example, is approximated by $(u_{i+1,j} - u_{i,j})/\Delta x = \chi_{i+1,j} - \chi_{i,j}$.

The time scale on which the thermal shock is modeled is much smaller than the characteristic time for thermal dissipation, and the system's temperature field can be considered as steady state. However, this argument does not exclude thermal shock behavior. A thermal shock is associated with a sudden localized temperature change in the monolith wall. These temperature changes can stem from light-off, hydrocarbon, or CO spikes in the feed or localized hot spots due to reaction front destabilization. Temperature changes need not only be temperature increases, but can also be sudden decreases in temperature, for instance, when a converter is suddenly cooled by changing driving conditions.

First, we will analyze the behavior of the system towards the formation of a hot spot. The displacement vector $(\chi_{i,j}, \gamma_{i,j})$ associated with a hot spot is as follows

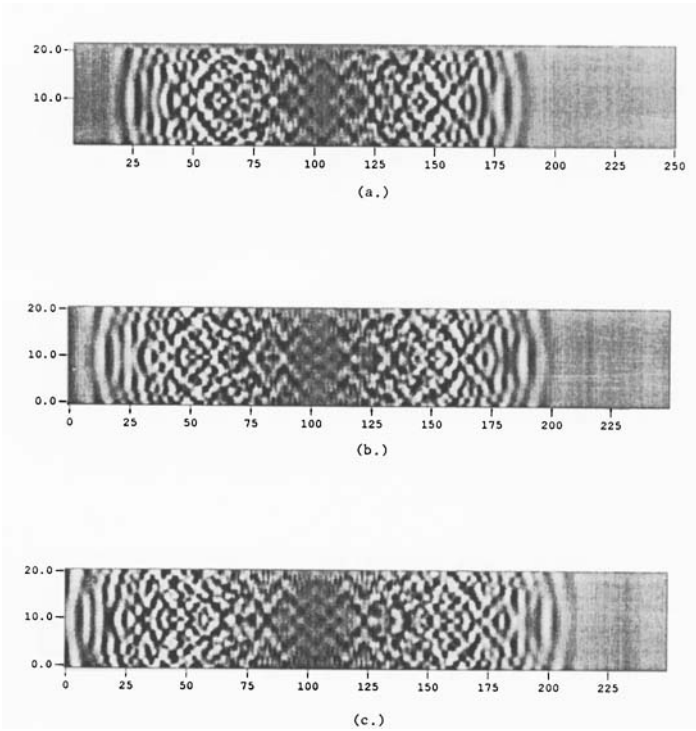

Figure 4. Shock waves in a flawless specimen.

$$\chi_{i,j} = -0.0003 \sin\left(2\pi \frac{(i-100)}{4}\right) \sin\left(\pi \frac{(j-9)}{4}\right) \tag{31}$$

$$\gamma_{i,j} = -0.0003 \sin\left(\pi \frac{(i-100)}{4}\right) \sin\left(2\pi \frac{(j-9)}{4}\right) \tag{32}$$

for $i \in [100, 104]$ and $j \in [9, 13]$. This perturbation is only a qualitative resemblance of real hot spots which may form, but it is plausible within the framework of a phenomenological model. The perturbation is sufficiently strong to snap springs.

Figure 4 shows the x-component of the displacement vector $\chi_{i,j}$ at $\tau = 4.0$, 4.5, and 5.0. All springs were intact before the shock occurred, which could be related to a system with a very small microcrack distribution. At $\tau = 4.0$, the waves have not reached either of the two free ends, but several have reflected from the top and bottom to form an interference pattern. Note the diminishing of waves in the region of the original perturbation. Springs have snapped in a cross-like pattern at the initial perturbation sites, indicative of quite a severe shock. No additional cracking was observed. At $\tau = 4.5$, the right traveling wave is located near column position $i = 190$ and the left traveling wave has reached the free end of the wall. At $\tau = 5.0$, a reflected wave is traveling away from the free boundary at left and interfering with incident waves. This causes local increases in amplitudes which is noticeable from a comparison between Figure 4b and Figure 4c.

To illustrate the effect of an existing microcrack distribution in the monolith support medium, the wall is randomly precracked by setting a certain percentage (10%) of spring constants equal to 0. The same perturbation has been used as before (i.e., Eq. 26). The x-component of the displacement vector in the wall is shown in Figure 5. No specific wave fronts are discernible, which indicates that the medium is much more dispersive. Comparing the shock pattern at $\tau = 4.0$ (Figure

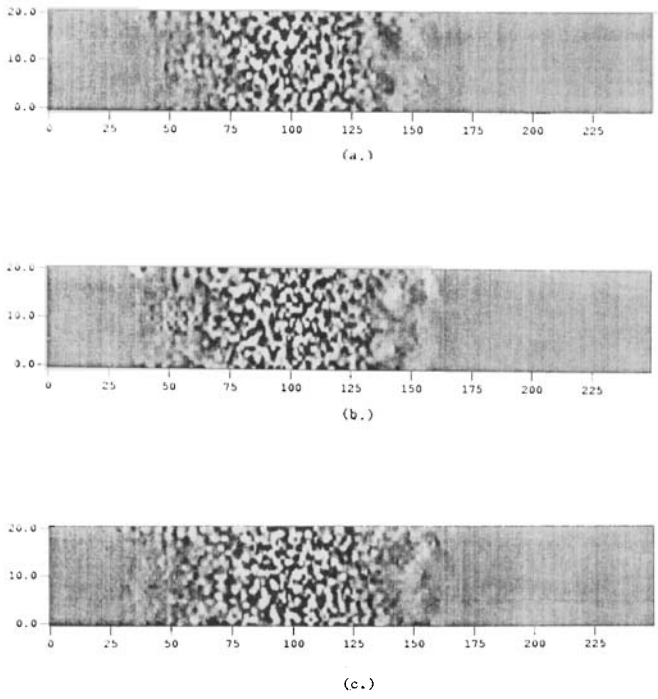

Figure 5. Shock waves in a precracked specimen.

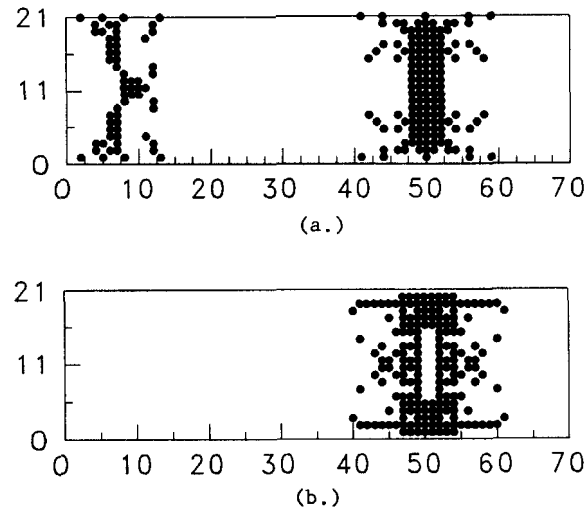

Figure 6. Broken springs in (a) *x* and (b) *y* directions.

5a) with the patterns at $\tau = 4.5$ (Figure 5b) and $\tau = 5.0$ (Figure 5c), one notices that the shock region has not expanded much. This region covers the width of the wall and extends from columns 25 to 175. Within this region, the shock waves are continuously scattered. Waves are also reflected from the top and bottom. Borrowing from fluid dynamics, one can describe this region as turbulent. Precracking has changed the shock behavior in two ways. It tends to contain the shock, and it destroys regular wave structures. When crack dimensions exceed the wavelength of the shock wave (in the direction of propagation), it acts as an internal free surface and incident waves are reflected. In contrast, smaller cracks scatter the waves more and their role can be better described as changing the macroscopic properties of the system (e.g., a decrease in the Young's modulus). The broken springs act as wave deflectors and the elastic energy cannot be transferred from one node to the next at the broken spring site.

Next, we want to model cracking when a compressional wave is incident on a free surface. Strong perturbations in the horizontal displacement components were applied at column 50 for rows 5–17. In Figure 6 the broken springs in the x and y directions are shown after the shock has dissipated. In the vicinity of the perturbations all the springs are broken, with small extensions at the corners of the perturbation region as well as along the fixed edges. The interesting result is the breakage that has occurred near the free boundary at left. This result is consistent with the phenomenon of spalling where an incident pressure wave is reflected as a tensile wave, and scabs can break off from the free surface. Also, note the shape of the crack pattern; it has the signature of the reflected wave and it is reminiscent of a sector of a circle. One can envisage that an extension to the third dimension will produce a fragment shaped like a spherical segment of one base. Although the wave amplitude has decreased considerably when it has reached the free end at left, the breaking criterion has been satisfied in this region. Additional insight as to why cracking occurs at the free end can be gleaned from the elastic energy of the system. Due to the fact that the first column of nodes has no supporting spring to the left, the initial displacement is greater when the shock wave reaches the free end compared to the displacements of the internal nodes. The subsequent oscillation of the end nodes is imparted to the neighboring internal nodes resulting in increasing displacements and hence higher elastic energy. The shock wave reaches the free end and the reflected wave is superimposed on incident waves which results in an increase of the elastic energy near the free end. The displacements of the internal nodes exceed the breaking condition and cracking is observed. In the y-direction, (Figure 6b) springs only broke in the vicinity of the perturbed region. Note that no springs snapped in the perturbed region itself, because the perturbation was only applied in the horizontal direction. Broken springs extend along the top and bottom edges. These cracks are parallel to each other and normal to the edges. This pattern is similar to the parking array patterns which were experimentally observed by Bahr et al. (1986).

The velocities of compressional and shear waves in precracked media are expected to be slower. In Figure 7 compressional waves are shown for the same perturbation as the flawless specimen presented in Figure 2. The change in the slopes of the characteristics is immediately evident and is indicative of a decrease in the propagation velocity. There is also a noticeable change in the wave patterns around the perturbed region. Scattering occurs and (although it cannot be assessed from the figures) the amplitudes are much smaller.

Conclusions

A model has been presented to describe shock propagation in a structure based on a node-spring representation of an elastic medium. The spring constants are related to the two elastic constants E_Y and ν. Within limits, the model can be adapted to model materials with anisotropic properties, local inclusions of foreign matter, and existing cracks. The boundary conditions can be defined for fixed, free, or external traction conditions. Viscous damping is included, but only elements on the diagonal of the viscosity tensor are considered, i.e., damping of shear propagation is not included. One prob-

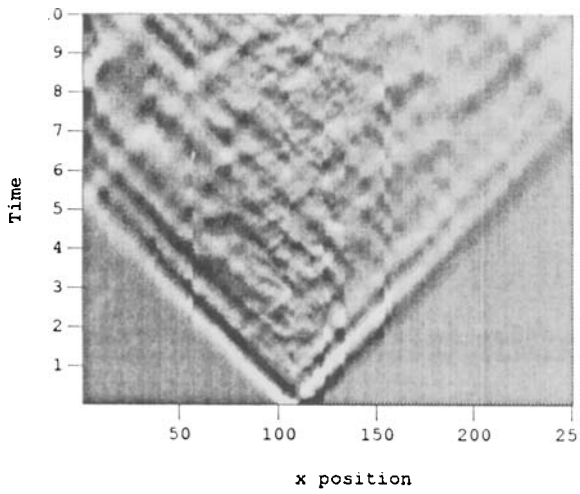

Figure 7. Compressional wave in pre-cracked medium.

lem in modeling damping is the scarcity of available data on damping coefficients. Velocities for shear and compressional waves calculated by the SNM model compare well with theoretical values.

An existing random distribution of microcracks decreases the elastic energy of the spring-node system. As a result, the applied thermal shock delivered to the system is more scattered and the resulting cracking of the matrix is less than in the flawless case. The presence of microcracks in the system is a result of the specimen history, and holds certain manufacturing implications. A fundamental description of damping is not yet at hand, and viscous damping is still the mechanism of choice. Whereas mechanisms like the Akhieser mechanism are used to describe attenuation in single crystals, damping in polycrystalline materials can more likely be attributed to scattering at the grain boundaries. With this in mind, materials processing, which could increase the grain boundary density, could also lead to a product with higher damping coefficients.

The presented model is simplistic and provides insight into the phenomenon of brittle fracture and factors that influence the propagation of cracks. Cracks are effectively considered as point defects in this model (single springs), and future work can include adding length to the cracks. Work-hardening at crack tips can be analyzed by changing the values of the spring constants in the vicinity of cracks. Initial displacement values can be defined to model different perturbations or shocks. The extension of this model to three-dimensional structures is straightforward, but the computational burden will increase considerably.

Acknowledgment

The authors gratefully acknowledge the financial support of the National Science Foundation through grant CTS-9308813.

Notation

C = damping coefficient, Ns/m^2
C_s = scale for damping coefficient, $\sqrt{k_s m/\Delta t^2}$
h = height of monolith wall, m
$k_s = E_Y \Delta t/500$
k_x = wavenumber in x-direction, 1/m
L = length of monolith wall, m
m = mass per node, kg
$p_{i,j,l}$ = integrity of spring l at nodal position, i, j
Q = dimensionless diagonal spring constant
t = time, s
$T_r = \sqrt{m/k_s}$
T_w = solid phase temperature, K
$u_{i,j}$ = displacement in x direction, m
$v_{i,j}$ = displacement in y direction, m
v_s = velocity of shear wave, m/s

Greek letters

ϵ = strain
κ = dimensionless spring constant k
ξ = dimensionless damping coefficient
ρ = density, kg/m^3
τ = dimensionless time

Subscripts

d = damping
e = equilibrium
s = diagonal

Literature Cited

Auld, B. A., *Acoustic Fields and Waves in Solids*, Wiley, New York (1982).

Bahr, H.-A., G. Fischer, and H.-J. Weiss, "Thermal-shock Crack Pattern Explained by Single and Multiple Crack Propagation," *J. Mater. Res.*, **21**, 2716 (1986).

Bennison, S. J., and B. R. Lawn, "Flaw Tolerance in Ceramics with Rising Crack Resistance Characteristics," *J. Mater. Sci.*, **24**, 3169 (1989).

Boley, B. A., and J. H. Weiner, *Theory of Thermal Stresses*, Wiley, New York (1960).

Cartz, L., *Nondestructive Testing*, ASM International, Materials Park, OH (1995).

Cherepanov, G. P., *Mechanics of Brittle Fracture*, McGraw-Hill, New York (1979).

Coble, R. L., and W. D. Kingery, "Effect of Porosity on Physical Properties of Sintered Alumina," *J. Amer. Cer. Soc.*, **39**(11), 377 (1956).

Coble, R. L., and N. M. Parikh, "Fracture in Polycrystalline Ceramics," in *Fracture. An Advanced Treatise, Vol. VII*, H. Liebowitz, ed., Academic Press, New York (1972).

Curtin, W. A., and H. Scher, "Brittle Fracture in Disordered Materials: A Spring Network Model," *J. Mater. Res.*, **5**(3), 535 (1990a).

Curtin, W. A., and H. Scher, "Mechanics Modeling Using a Spring Network," *J. Mater. Res.*, **5**(3), 554 (1990b).

Curtin, W. A., and K. Futamura, "Microcrack Toughening," *Acta Metall. Mater.*, **38**(11), 2051 (1990).

Dörre, E., and H. Hübner, *Alumina, Processing, Properties and Applications*, Springer-Verlag, New York (1984).

Hasselman, D. P., "Analysis of the Strain at Fracture of Brittle Solids with High Densities of Microcracks," *J. Am. Cer. Soc.*, **52**(8), 458 (1969).

Kam, T. Y., and C. D. Lu, "Thermal Stress Fracture Analysis of Brittle Bodies," *Eng. Fracture Mech.*, **32**(5), 827 (1989).

Leclerc, J. P., and D. Schweich, "Modeling Catalytic Monoliths for Automobile Emission Control," in *Chemical Reactor Technology for Environmentally Safe Reactors and Products*, H. I. De Lasa et al., eds., Kluwer Academic Publishers, Dordrecht, The Netherlands, p. 547 (1993).

Prantskyavichyus, G. A., "Role of Structure and Capacity for Energy Adsorption in Increasing the Strength and Crack Resistance of Refractory Ceramics," *Refractories*, **28**(7–8), 362 (1987).

Taylor, K. C., *Automobile Catalytic Converters*, Springer-Verlag, Berlin-New York (1984).

Villermaux, J., and D. Schweich, "Is the Catalytic Monolith Reactor Well Suited to Environmentally Benign Processing?," *Ind. Eng. Chem. Res.*, **33**, 3025 (1994).

Zygourakis, K., "Transient Operation of Monolith Catalytic Converters: a Two-Dimensional Reactor Model and the Effect of Radially Nonuniform Flow Distributions," *Chem. Eng. Sci.*, **44**(9), 2075 (1989).

Manuscript received Dec. 11, 1995, and revision received May 9, 1996.